Photosystem I-based Biophotovoltaics on Nanostructured Hematite

Kasim Ocakoglu, Tomasz Krupnik, Bart van den Bosch, Ersan Harputlu, Maria Pia Gullo, Julian David Janna Olmos, Saadet Yildirimcan, Ram K. Gupta, Fahrettin Yakuphanoglu, Andrea Barbieri, Joost N. H. Reek, and Joanna Kargul**

The electronic coupling between a robust red algal photosystem I (PSI) associated with its light harvesting antenna (LHCI) and nanocrystalline n-type semiconductors, TiO_2 and hematite (α-Fe_2O_3) is utilized for fabrication of the biohybrid dye-sensitized solar cells (DSSC). PSI-LHCI is immobilized as a structured multilayer over both semiconductors organized as highly ordered nanocrystalline arrays, as evidenced by FE-SEM and XRD spectroscopy. Of all the biohybrid DSSCs examined, α-Fe_2O_3/PSI-LHCI biophotoanode operates at a highest quantum efficiency and generates the largest open circuit photocurrent compared to the tandem system based on TiO_2/PSI-LHCI material. This is accomplished by immobilization of the PSI-LHCI complex with its reducing side towards the hematite surface and nanostructuring of the PSI-LHCI multilayer in which the subsequent layers of this complex are organized in the head-to-tail orientation. The biohybrid PSI-LHCI-DSSC is capable of sustained photoelectrochemical H_2 production upon illumination with visible light above 590 nm. Although the solar conversion efficiency of the PSI-LHCI/hematite DSSC is currently below a practical use, the system provides a blueprint for a genuinely green solar cell that can be used for molecular hydrogen production at a rate of 744 µmoles H_2 mg Chl^{-1} h^{-1}, placing it amongst the best performing biohybrid solar-to-fuel nanodevices.

1. Introduction

Direct conversion of solar energy into the condensed chemical energy of storable fuels within a nanoscale synthetic system is an attractive goal. However, achieving the required stability, efficiency and cost-effectiveness of such fully integrated devices remains the main challenge. On the other hand, nature has optimized the process of solar energy conversion into energy of chemical bonds with the evolution of oxygenic photosynthesis. This fundamental process by which solar energy is harnessed and converted to condensed energy of chemical bonds operates on a truly global scale, sustaining life on Earth. In this way, natural photosynthesis provides not only a source of oxygen, biomass, food and fossil fuels, but it can capture an average of 120 TW of solar energy reaching our Planet daily, largely exceeding the current global annual energy demand of ~16 TW.[1] Despite a low

K. Ocakoglu, E. Harputlu, S. Yildirimcan
Advanced Technology Research and Application Center
Mersin University
Ciftlikkoy Campus
TR-33343, Mersin, Turkey
E-mail: kasim.ocakoglu@mersin.edu.tr

T. Krupnik, J. D. J. Olmos, J. Kargul[+]
Department of Plant Molecular Physiology
Faculty of Biology
University of Warsaw
Miecznikowa 1, 02–096, Warsaw, Poland
E-mail: j.kargul@biol.uw.edu.pl

B. van den Bosch, J. N. Reek
Van t Hoff Institute for Molecular Sciences
University of Amsterdam
POSTBUS 94720, 1090, GS, Amsterdam, The Netherlands

[+]Center of New Technologies, University of Warsaw, Banacha 2C, 02–097 Warsaw, Poland

M. P. Gullo, A. Barbieri
Istituto per la Sintesi Organica e la Fotoreattività (ISOF)
Consiglio Nazionale delle Ricerche (CNR)
Via Gobetti 101, 40129, Bologna, Italy

R. K. Gupta
Department of Chemistry
Pittsburg State University
Pittsburg, KS 66762, USA

F. Yakuphanoglu
Department of Physics
Faculty of Science
Firat University
TR-23119, Elazıg, Turkey

DOI: 10.1002/adfm.201401399

© 2014 WILEY-VCH Verlag GmbH & Co. KGaA, Weinheim

energy conversion efficiency of natural photosynthesis (average of 0.2% solar-to-dry biomass), the overall amount of solar energy converted photosynthetically into dry biomass accounts for approximately ten times the total amount of energy used by humans annually.[2]

The early events of oxygenic photosynthesis: light harvesting, charge separation and charge transfer are conducted by two large multimeric pigment-protein complexes, photosystem I (PSI) and photosystem II (PSII), that are embedded within the thylakoid membranes of higher plants, algae and cyanobacteria. PSII and PSI work in tandem by capturing photons from the visible solar spectrum with chlorophyll (Chl) molecules and utilizing the energy of the absorbed photons to generate spatially separated electron–hole pairs. The holes are stored by the catalytic center of PSII, the oxygen-evolving complex to oxidize water to oxygen and reducing equivalents, whereas the electrons are stored in chemical bonds by PSI to reduce nicotinamide adenine dinucleotide phosphate (NADP) to NADPH and in the form of adenosine triphosphate (ATP).

Both PSII and PSI are structurally organized around the common blueprint, whereby they both contain a reaction center (RC) coupled to a light harvesting complex (LHC) that binds several hundred Chl and carotenoid molecules.[3,4] The energy of photons captured by the LHCs of PSII and PSI is rapidly transferred to the photochemical RCs, the P680 and P700 Chl*a* molecules, respectively, where it is converted to the charge separation state followed by the vectorial flow of electrons and protons across a membrane.[3]

In PSI, absorption of red photons by P700 RC (E_m + 0.43 eV) leads to formation of the highly reducing excited state P700* (a dimer of Chl*a* molecules with E_m – 1.3 eV), which is then rapidly oxidized to $P700^+$ as it ejects an electron down the energy gradient through a structurally conserved chain of redox active cofactors, including Chls, phylloquinones and 3 iron-sulfur [4Fe-4S] clusters. The terminal electron acceptor is formed by the special iron-sulfur cluster, termed F_B (E_m – 0.58 eV), which is located on the stromal (acceptor) side of the complex, and which donates an electron to the natural electron acceptor, ferredoxin. On the other hand, re-reduction of the $P700^+$ species on the lumenal (donor) side is facilitated by the natural electron donor, plastocyanin or cytochrome c_6. The final light-induced redox potential difference between the primary electron donor P700* and the terminal electron acceptor F_B^- is about 1 V, corresponding to a thermodynamic efficiency of nearly 60%.[5]

As oxidation and reduction of the redox partners occur on the opposite sides of the thylakoid membrane, PSI has to provide an efficient electron transfer pathway across the membrane.[6] Indeed, despite high structural complexity (12–17 protein subunits and 127–178 cofactors for the cyanobacterial and higher plant PSI complexes,[7–9] PSI operates with a quantum yield of charge separation close to unity and as yet, no synthetic system approached this remarkable efficiency. This means that each quantum of light that reaches P700 RC creates the primary radical pair species and ultrafast charge separation within a few picoseconds followed by charge transfer to the terminal electron acceptor within 1 µs.[10,11]

As photoexcitation of PSI generates a considerable amount of free energy, this robust and highly abundant photoactive protein complex PSI provides an attractive candidate for nanoscale engineering of the biohybrid photovoltaic (PV) and photoelectrochemical (PEC) devices.[5,12–18] PSI forms a long-lived charge-separated state $P700^+F_B^-$ (~60 ms) and is characterized by an exceptionally low redox potential associated with the distal F_B cluster, therefore in principle, it provides a sufficient driving force to reduce protons to H_2 at neutral pH.[1,19] On the other hand, the versatile nature of PSI to act both as an acceptor ($P700^+$) and as a donor (F_B^-) of electrons allows for this complex to be applied for generation of both anodic and cathodic photocurrents.[17]

The construction of efficient biohybrid PSI-based PEC or PV cells can only be realized if all the components are redox compatible, a fast directional electron transfer pathway exists between the immobilized PSI complex and the electrode surface, and a sufficient amount of the nanostructured photoactive PSI complex is deposited on the electrode. Another important consideration is to minimize energy losses due to the diffusion-based electron transfer and charge recombination (back) reactions. Although in PSI formation of the charge separated state is nearly irreversible, if this protein complex is not properly oriented on the electrode surface both charge recombination and short circuiting of electron transfer between anisotropically oriented PSI complexes are likely to occur. To overcome this problem several strategies have been adopted including oriented covalent cross-linking of PSI to the functionalized electrode surfaces, wiring of PSI to the electrode and integrating physisorbed PSI particles as a thick multilayer onto the electrodes. Das et al. demonstrated efficient oriented integration of the His-tagged higher plant PSI stabilized by the surfactant peptides into Ni-NTA-functionalized Au/ITO electrode coupled with an organic semiconductor tris(8-hydroxyquinoline) aluminum, generating the biohybrid PV devices that produced photocurrent for several weeks in ambient conditions.[12] In a different approach, Jennings and colleagues achieved oriented covalent immobilization of the higher plant PSI monolayer (with P700 proximal to the electrode) on thiolated gold surfaces by vacuum adsorption, reporting photocurrent densities of up to 100 nA cm^{-2} mW^{-1}, using the free diffusing redox mediator 2,6-dichloroindophenol (DCIP) as electron acceptor and ascorbate as the sacrificial electron donor.[20] In the follow-up studies the same group reported a significantly increased photocurrent of 0.4 mA cm^{-2} mW^{-1} when PSI was deposited as a thick multilayer on nanoporous gold or glass electrodes,[14–16] demonstrating the importance of smart nanostructuring of the PSI layer for a markedly increased PV performance. Oriented immobilization of PSI via its acceptor side was also achieved by reconstitution of photocatalytical activity of phylloquinone (A1)-depleted PSI on a naphthoquinone-modified gold surface, yielding current densities of up to 120 nA cm^{-2} mW^{-1}.[21,22] This elegant approach allowed for short-circuiting of the photo-induced electron transfer directly from the A1 site of PSI to the electrode, thus bypassing the natural electron transfer to the terminal F_B cluster. In an alternative approach, Yehezkeli et al. reported the photocurrent density to date of up to 1.38 µA cm^{-2} mW^{-1} by using bis-aniline cross-linking of platinized PSI and ferredoxin particles with electrodes,[23] demonstrating the importance of limiting charge recombination and fast forward electron transfer within PSI for the enhanced photocurrent generation in such biophotovoltaic devices.

© 2014 WILEY-VCH Verlag GmbH & Co. KGaA, Weinheim

Recently, Rögner and colleagues reported efficient integration of cyanobacterial PSI with a gold electrode by using an Os(II)/(III)-modified redox polymer hydrogel which served both as a scaffolding matrix and non-diffusible electron donor to photooxidised PSI.[18] Such a device yielded the significantly improved photocurrent density of 29 μA cm^{-2} mW^{-1} when methyl viologen was used as the artificial electron acceptor of PSI, demonstrating the importance of fast non-reversible electron transfer between the photoactive PSI complex and the electrode for an improved PV conversion efficiency.

Because of the intrinsic light harvesting and redox properties of PSI, integration of this photoactive macromolecular complex with an appropriate, redox tuned-in semiconductor electrode provides an attractive approach for fabrication of biohybrid photo-optical cells, e.g., dye-sensitized solar cells (DSSCs), of significantly improved efficiencies. In such biohybrid applications two particular semiconductor substrates, TiO_2 (anatase) and α-Fe_2O_3 (hematite), have attracted considerable interest due to their ability to absorb visible light and the photocatalytical properties. TiO_2 has been used in photocatalysis and photovoltaics because of its combination of energy band structure, carrier transport, and stability. However, wide band gap and relative slow carrier transport limits its full potential in these applications. 3.2 eV band gap of anatase indicates its low efficiency of utilizing full spectrum of solar light. On the other hand, α-Fe_2O_3, being a narrow band gap *n*-type semiconductor (2.1 eV band gap) has been the material of choice for construction of DSSCs due to its non-toxicity, widespread availability, low-cost, superior stability against photocorrosion and extensive absorption in the visible part of the light spectrum.[24,25] Recently, nanostructured hematite has attracted considerable interest through its application in the hydrogen producing PEC devices and DSSCs.[26–28] Nanoparticles of hematite were used to improve the efficiency of solar-to-electric energy conversion from 2.8% to 3.7%,[29] albeit with enhanced optical absorption due to the surface plasmon effect.[30]

Recently, Mershin and colleagues reported a promising application of stabilized cyanobacterial PSI as a biophotoanodic component of a biohybrid DSSC.[31] In the latter work, PSI, being an intrinsically efficient light-harvesting and charge separator, was energetically coupled with the TiO_2 or ZnO semiconductor substrates, albeit operating at rather modest solar-to-electric quantum efficiencies of 0.03% or 0.08%, respectively. The cells consisted of a native or modified PSI complex whose native PsaE stromal subunit was replaced with a recombinant PsaE counterpart containing a ZnO-binding peptide. Such reconstituted PSI was positioned on the semiconductor surface/nanowires with the acceptor side close to the electrode, either by physisorption (TiO_2) or selective adsorption using ZnO-binding peptide motifs. Upon excitation, and using Co(II)/(III)-tris-bipyridine as the electrolyte/electron transfer mediator, the photogenerated $P700^+$ hole was scavenged by the reduced cobalt complex, which, in turn, was regenerated by the Pt cathode. This DSSC device operated at open circuit photovoltage of 0.5 V, fill factor of 71%, electrical power density of 81 μW cm^{-2} and photocurrent density of 362 μA cm^{-2}, representing over four orders of magnitude better performance compared to all previously reported PSI-based biophotovoltaic devices.[31]

Here, we report a construction of a fully integrated, stable and functional PSI-based biohybrid DSSC with over 2-fold improved solar-to-electric quantum efficiency over the biohybrid device reported previously by Mershin and colleagues.[31] The biohybrid anodic component of our device comprised two *n*-type semiconductor substrates, hematite or TiO_2, which were coupled with an oriented nanostructured multilayer of a highly robust PSI-LHCI supercomplex purified from an extremophilic red microalga *Cyanidioschyzon merolae*. By manipulating surface charge distribution of the PSI-LHCI complex we oriented it with the acceptor (reducing) side close to the mesoporous hematite surface of the photoanode. The hematite–PSI-LHCI assembly showed a significantly increased photocurrent and quantum efficiency of solar energy conversion in comparison with the analogous device constructed with a TiO_2–PSI photoanode. We attribute this increase to the enhanced light absorption and charge separation within hematite after oriented integration of the fully active PSI-LHCI complex which serves as a natural photosensitizer for this semiconductor substrate. The biohybrid nanostructured PSI-hematite DSSC assembly showed a long-term stability of up to 90 days. Importantly, it was capable of sustained photoelectrochemical H_2 production upon illumination with red visible light, and as such it constitutes a promising truly green biohybrid system for solar-to-fuel conversion.

2. Results and Discussion

2.1. Nanostructuring of the Semiconductor Substrates

Efficient interaction between the photosensitizer and semiconductor provides more effective charge transfer resulting in the enhancement of the overall power conversion efficiency. Moreover, 3D organization of the photoelectrode surface plays an important role in the energy conversion and charge transfer efficiency.[32–34] A general approach is to modify the flat surface of the electrode with nanostructured mesoscopic semiconductor materials which contain large surface area junctions between photoelectron donors and acceptors. The nanoarchitecture of highly ordered nanostructured metal oxide semiconductors was shown to be effective for photoelectrochemical H_2 generation and sensing, as well as photocatalytic CO_2 reduction into hydrocarbon-based liquid fuels.[35,36]

Led by these observations, we first engineered highly ordered nanocrystalline structures of α-Fe_2O_3 and TiO_2 semiconductors aiming at enhancing their absorption and photocatalytical properties by efficient integration of a highly robust natural photosensitizer/charge separator, the PSI-LHCI supercomplex from a red extremophilic microalga *Cyanidioschyzon merolae*. X-ray diffraction (XRD) analysis confirmed the hexagonal phase of α-Fe_2O_3 that provided the semiconductor substrate for subsequent nanoengineering of the biohybrid photoelectrode (see Figure S1). Field-emission scanning electron microscopy (FE-SEM) imaging of the semiconductor nanostructure showed that α-Fe_2O_3 and TiO_2 nanocrystals formed a uniform film over fluorine-doped tin oxide (FTO) glass plate (see Figure S2).

© 2014 WILEY-VCH Verlag GmbH & Co. KGaA, Weinheim

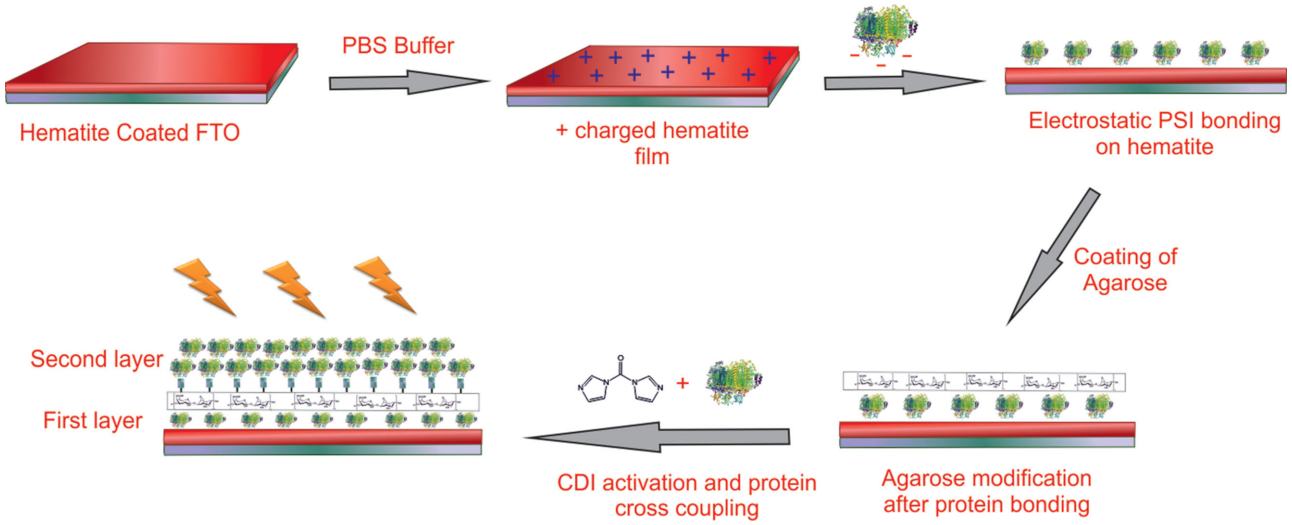

Figure 1. Schematic diagram for fabrication of PSI/α-Fe_2O_3/FTO electrode. FTO glass plate was covered with nanostructured mesoporous hematite. PSI multilayer was physisorbed at pH 4 onto the hematite film with its reducing side in the proximity of the semiconductor. Subsequent coating with agarose provided an interface for chemical crosslinking with 1,1′-carbonyldiimidazole (CDI) to attach a second multilayer of PSI in the head-to-tail orientation upon immobilisation at pH 4.

2.2. Construction of the PSI-based DSSCs

Following construction of mesoscopic, high-surface area electrodes composed of nanostructured α-Fe_2O_3 and TiO_2 semiconductor substrates of varying band gaps, we aimed at enhancing their absorption cross-section properties by functional integration of oriented highly robust and homogeneous *C. merolae* PSI-LHCI particles.

To construct the biohybrid DSSCs, oriented *C. merolae* PSI-LHCI particles were physisorbed at pH 4 and pH 7.4, then covalently cross-linked as a multilayer on nanostructured semiconducting substrate (**Figure 1**), and the electric circuits were completed by liquid electrolyte ($3I^-/I_3$) and platinized FTO glass, forming sandwich-type cells (**Figure 2**). As seen in the energy flow diagram depicted in **Figure 3**, PSI-LHCI immobilized over each semiconductor absorbs the incident red photons which in turn excite the P700 RC to a highly reducing excited state P700*. The electrons from the P700* excited state are then transferred to the conduction band of each semiconductor, resulting in generation of anodic photocurrents. The electrons from the conduction band of each semiconductor are ultimately injected into the FTO layer.

Figure 4 and **Table 1** show the *I–V* characteristics of various fabricated solar cells, and their photovoltaic performance, including short-circuit currents (J_{sc}), open-circuit voltages (V_{oc}), fill factors (*FF*) and overall conversion efficiencies (η). Of all the biohybrid devices constructed, the solar cell in which the photoanode was composed of PSI-LHCI/α-Fe_2O_3/FTO, in which PSI-LHCI was immobilized at pH 4, gave the best performance, with current densities of up to 56.9 μA cm^{-2} and the solar energy conversion efficiency (η) of up to 0.17% under standard air-mass 1.5 (AM 1.5) sunlight, a value over 2-fold higher than that of the PSI-based DSSC reported by Mershin and colleagues.[31] The relatively low V_{oc} obtained in this study for the PSI-LHCI/α-Fe_2O_3/FTO solar cell compared to the device of

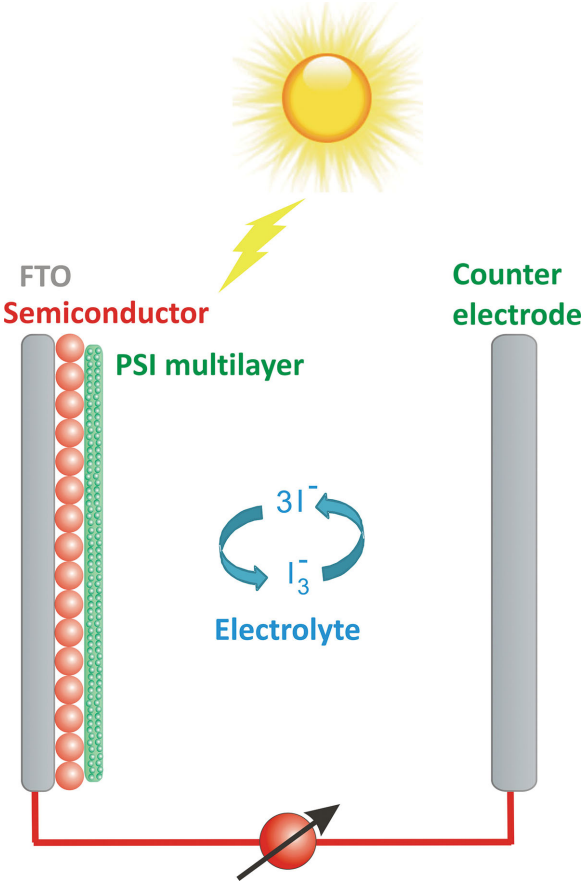

Figure 2. Schematic representation of fabricated solar cells. Oriented *C. merolae* PSI-LHCI particles were physisorbed and covalently cross-linked as a multilayer on nanostructured semiconducting substrates, and the electric circuits were completed by liquid electrolyte ($3I^-/I_3^-$) and platinized FTO glass, forming sandwich-type cells.

© 2014 WILEY-VCH Verlag GmbH & Co. KGaA, Weinheim

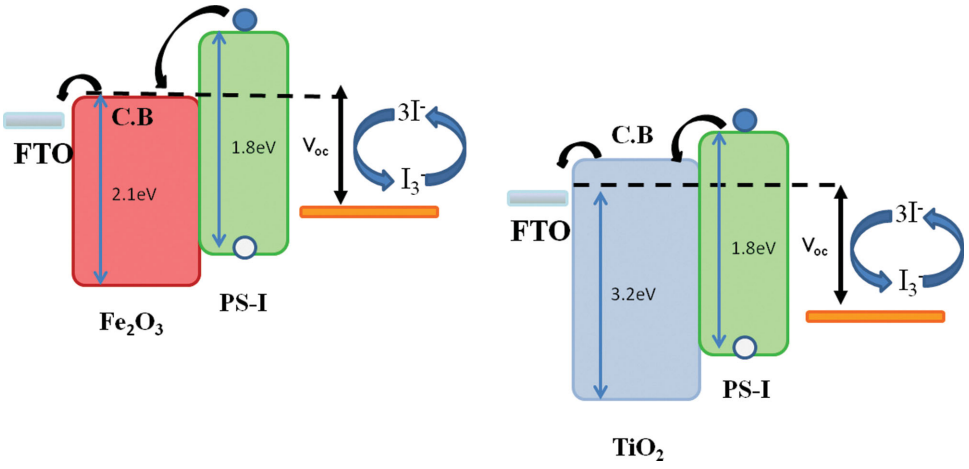

Figure 3. Energy band diagrams of fabricated solar cells. PSI-LHCI immobilized over each semiconductor absorbs the incident red photons which in turn excite the P700 RC to a highly reducing excited state P700* ($E_m = -1.3$ eV). The electrons from P700* are then transferred to the conduction band (C.B.) of each semiconductor, albeit with 2-fold smaller energy gradient for TiO_2 compared to hematite. As a result, anodic photocurrents are generated. The electrons from C.B. of each semiconductor are ultimately injected into the FTO layer. The positive holes ($P700^+$) are scavenged by the electrolyte.

Mershin et al. composed of ZnO/PSI anode[31] is most likely due to the use of a different electrolyte system.

In DSSCs, the photovoltage is determined by the difference between the quasi Fermi level of a semiconductor and the redox potential of the electrolyte. The lower conduction band potential of α-Fe_2O_3 (compared to TiO_2) makes electron injection from the sensitizer into the conduction band of semiconductor more thermodynamically favorable. This characteristic is particularly useful for increasing the electron injection rate of sensitizers; however, it also reduces the open circuit voltage (V_{oc}). Using the PSI-LHCI/α-Fe_2O_3/FTO photoanode, (with PSI immobilized at pH 4) the device exhibits 60-fold increase of the anodic photocurrent (J_{sc} = 56.9 μA) compared to the device with PSI-LHCI/TiO_2/FTO electrode (J_{sc} = 0.94 μA), while maintaining a V_{oc} of 321 mV. It is clear that the conduction band of α-Fe_2O_3 is better matched energetically with photoexcited P700* compared to TiO_2 (Figure 3), which explains better overall power conversion efficiency of the PSI-LHCI/α-Fe_2O_3 system compared to the cell with PSI-LHCI/TiO_2 photoanode. The additional reason for the strongly diminished photocatalytical activity of the latter photoanode is the less favorable orientation of the PSI-LHCI multilayer with respect to the TiO_2 surface under the pH conditions used, as explained in detail in Section 2.3. Consequently, the orientation of the PSI-LHCI layer on does not favor an efficient electron transfer from PSI-LHCI to TiO_2 electrode, which provides the additional reason for the lack of a significant photocatalytical activity of the latter.

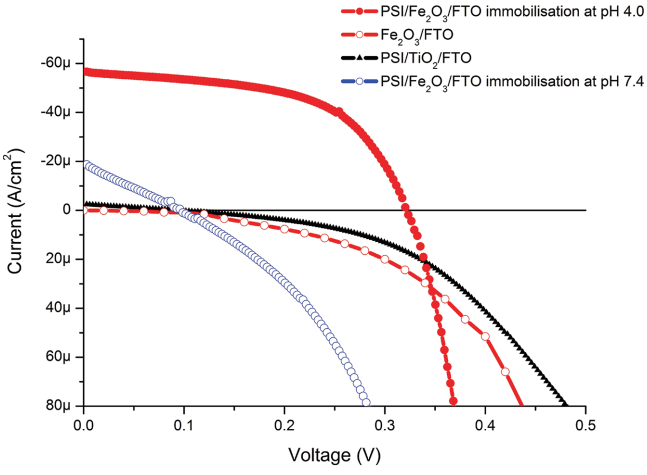

Figure 4. *I–V* characteristics of various fabricated PSI-based DSSCs. Measurements were conducted at AM1.5 irradiation (100 mW/cm^2) and with a long-pass filter >590 nm to eliminate light absorption by hematite. Two configurations of biohybrid PSI-based photoanodes were tested: PSI/α-Fe_2O_3-coated FTO electrode (red and blue) and PSI/TiO_2-coated FTO electrode (black). Of all the photoanodes tested, PSI/α-Fe_2O_3/FTO (PSI immobilized at pH 4) yielded the highest overall quantum efficiency (η = 0.17%), the highest fill factor (FF = 0.56) and the largest anodic photocurrent (J_{sc} = 56.9 μA). The control photoanode α-Fe_2O_3/FTO showed no detectable photocurrent.

It is known that the optical properties of the hematite film are strongly affected by the annealing temperature. As an example, Sivula and colleagues demonstrated that the absorption coefficient of the hematite film increased when the annealing temperature was raised from 400 °C to 800 °C, due to enlargement of the particle size.[37] It was therefore important to eliminate the possibility of changes in absorption properties of the hematite film that was annealed at 550 °C in our study. As shown in Figure S3, the nanocrystalline hematite/FTO film does not exhibit significant absorption above 590 nm, in contrast to PSI-LHCI which shows a maximum absorption at 680 nm in the red region. However, the residual absorption of hematite above 590 nm (likely due to d-d transitions) should also be taken into account when evaluating the performance of hematite-based

Table 1. Photovoltaic properties of fabricated solar cells.

Solar cell	J_{sc}, μA	V_{oc}, mV	*FF*	η,%
PSI/TiO_2/FTO	0.94	260	0.60	0.026
PSI/Fe_2O_3/FTO[a)]	56.9	321	0.56	0.170
PSI/Fe_2O_3/FTO[b)]	18.7	295	0.38	0.021

[a)]PSI immobilization at pH 4; [b)]PSI immobilization at pH 7.4.

© 2014 WILEY-VCH Verlag GmbH & Co. KGaA, Weinheim

Table 2. Photoelectrochemical activity of *C. merolae* LHC-PSI immobilized on hematite.

	Physisorbed PSI/hematite	Cross-linked PSI/hematite	PSI in solution pH 8	PSI in solution pH 4	PSI in solution pH 4[c)]
Activity, μmoles O_2/mg Chl/h	873.2 ± 103	900.9 ± 84[a)]	942 ± 127	707.8 ± 36	630 ± 3.6
		1923.6 ± 560[b)]			

The activity was measured 90 days after preparation of the electrodes. [a)]PSI immobilization at pH 7.4; [b)]PSI immobilization at pH 4; [c)]PSI was incubated at pH 4 then transferred to pH 8 to estimate recovery of the photochemical activity.

DSSCs.[37,38] To this end, we compared the photovoltaic properties of α-Fe_2O_3/FTO-based DSSC with those of PSI-LHCI-α-Fe_2O_3/FTO solar cell under identical experimental conditions. An extended absorption spectrum of hematite was eliminated by using a long-pass filter with a 590 nm cut-off wavelength during simultaneous measurements. As shown in Figure 4, α-Fe_2O_3/FTO film did not produce any significant photocurrent when the cut-off filter was used, thus confirming that photovoltaic activity of PSI-LHCI/α-Fe_2O_3/FTO photoanode can be attributed solely to the light absorption of the PSI-LHCI acting as a natural photosensitizer of hematite in the spectral range of 590–750 nm.

2.3. Investigation of Photochemical Activity and Nanostructuring of PSI-LHCI Layer on Mesoporous Hematite

To ensure optimal operation of the fabricated biohybrid PSI-LHCI/hematite-based DSSC it was important to efficiently integrate the photochemically active and stable PSI-LHCI complex that was energetically coupled with the conduction band of hematite, thus extending the light absorption spectrum of this semiconductor substrate into the red region. To this end, we used a highly robust and photochemically active PSI-LHCI complex purified to homogeneity from an extremophilic red microalga *Cyanidioschyzon merolae*. This supercomplex of 640 kDa consists of the RC domain (where the P700 Chl*a* dimer and all the electron transport cofactors are located) and an asymmetrically located crescent of Lhcr light harvesting subunits bound on the PsaF side.[39] The purified PSI-LHCI complex showed photochemical activity of 942 ± 127 μmoles O_2 mg Chl^{-1} h^{-1} and 708 ± 36 O_2 mg^{-1} Chl h^{-1} at pH 8 and 4 respectively, as measured by the O_2 consumption assay (see **Table 2**). Photochemical activity of *C. merolae* PSI subjected to pH 4 was fully restored upon transfer of this complex to pH 8 (Table 2), a pH value close to the pH optimum for this complex (pH 9, data not shown).

In our experiments, preparation of an efficient biophotoanode strongly depends on the formation of a positively charged semiconductor surface following its treatment with the phosphate buffer solution, pH 7.4. During the electrostatic conjugation process, the hematite surface becomes positively charged due to the environmental pH being below the isoelectric point of hematite (pI 8.4–8.5).[40] In contrast, the isoelectric point of anatase TiO_2 is between 5.0–5.5,[41] therefore the net anatase surface charge is negative under our experimental conditions.

In order to efficiently integrate PSI-LHCI with the semiconductor electrode we took advantage of the inherent asymmetric surface charge distribution within this macromolecular complex at various pH. We calculated the surface charge maps of the RC domain of PSI at pH 4 and 7, using the coordinates of the cyanobacterial PSI complex for which a near-atomic 2.5 Å X-ray structure is available.[7] **Figure 5** shows significant changes in the surface charge distribution upon transition from pH 7 to pH 4. At pH 7 (Figure 5A) the P700 (donor) side of the PSI complex is predominantly negatively charged (net charge of –0.54 V), while the acceptor side is nearly neutral (net charge of +0.04 V), resulting in significant polarization of the PSI complex (with an average charge difference of about 0.58 V). Upon transition to pH 4 (see Figure 5B) the acceptor (reducing) side of PSI becomes positively charged (net charge of +0.53 V) and the donor side becomes less negative (net

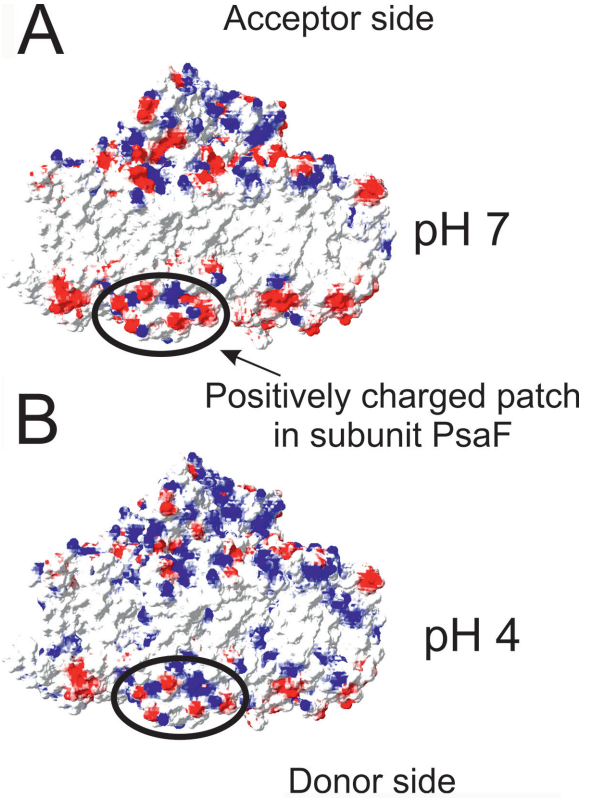

Figure 5. Surface charge distribution maps of *Synechococcus elongatus* PSI[7] at A) pH 7 and B) pH 4. Residues rendered in red and blue carry negative and positive charge, respectively. Calculation were performed with the values of dielectric constant of solvent $\varepsilon = 80$ and protein $\varepsilon = 4$. Ionic strength was 0.1 mol l^{-1}.[48] PsaF subunit is circled in (A), and its positively charged patch is indicated with an arrow amidst largely negatively charged surface of the donor side at pH 7. The average surface potential of the donor side was $q_{pH\ 7} = -0.537$ V and $q_{pH\ 4} = -0.145$ V, whereas for the acceptor side the average potential was estimated at $q_{pH\ 7} = +0.046$ V and $q_{pH\ 4} = +0.534$ V, respectively.

© 2014 WILEY-VCH Verlag GmbH & Co. KGaA, Weinheim

charge of –0.14 V), building up even a greater charge difference of about 0.67 V. Therefore, at pH 4 and upon illumination with visible light PSI-LHCI is likely to be oriented preferentially with its reducing side towards the positively charged hematite surface due to neutralization of negative charge of the donor side and the flow of photoexcited electrons from P700 RC towards the F_B cluster on the acceptor side of the complex. This is in contrast to PSI-LHCI immobilized on hematite at pH 7.4, in which the donor side becomes negative, resulting in its preferential orientation towards the positively charged electrode (see Figure 5A). Similarly, electrostatic repulsion between the negatively charged acceptor side of PSI-LHCI incubated in the light at pH 4 and the negatively charged pre-treated TiO_2 electrode likely results in unfavorable orientation of the PSI-LHCI layer with respect to the TiO_2 semiconductor surface, thus limiting efficient electron transfer and overall performance of this photoanode. It is important to emphasize that a more direct proof of such pH-dependent polarized orientation of PSI-LHCI with respect to the hematite surface remains to be established, and will be a subject of future studies.

We then proceeded to investigate geometry of the PSI-LHCI multilayer upon its integration with the hematite/FTO electrode at pH 4. **Figure 6** shows top and cross-sectional FE-SEM images of α-Fe_2O_3-coated FTO templates containing immobilized *C. merolae* PSI-LHCI. The cross-section FE-SEM imaging of the PSI-LHCI/α-Fe_2O_3/FTO electrode reveals the detailed 3D organization of the PSI-LHCI multilayer, with a total thickness of about 165 nm (Figure 6C). This multilayer is likely to comprise ~15 physisorbed and chemically cross-linked monolayers, assuming a thickness of the cyanobacterial PSI in the membrane plane of 10.6 nm.[7]

Importantly, photochemical activity of PSI-LHCI that was physisorbed or chemically cross-linked with the mesoporous hematite at pH 4 was comparable with the activity measured in solution (see inset to **Figure 7** and Table 2), indicating that the PSI-LHCI complex retained its full functionality upon integration within the semiconductor surface. At pH 7.4, the physisorbed and covalently cross-linked PSI-LHCI immobilized on the hematite surface exhibited unchanged photochemical activity. Interestingly, the photochemical activity of the cross-linked PSI-LHCI multilayer adsorbed to the hematite surface at pH 4 doubled, most likely due to the highly ordered macromolecular arrangement of the PSI-LHCI multilayer in which stronger surface charge polarization may induce donor-to-acceptor side (head-tail) orientation of this complex in the consecutive PSI monolayers, as shown in Figure 6C and schematically depicted in Figure 1. Moreover, the long-term activity of the PSI complex was sustained over the period of at least 90 days following its integration with the hematite surface (Table 2).

Steady-state 77 K and RT fluorescence spectroscopy additionally confirmed that the PSI-LHCI complex largely retained its energy transfer properties upon integration with a hematite photoanode. We observed a 4–12 nm shift of the 77K emission maxima towards the blue region upon immobilization of PSI on the hematite electrode (see Figure 7) most likely due to changes in Chl-protein interaction upon adsorption or cross-linking of PSI with functionalized hematite. A similar phenomenon was observed for photoactive *C*-phycocyanin upon its covalent

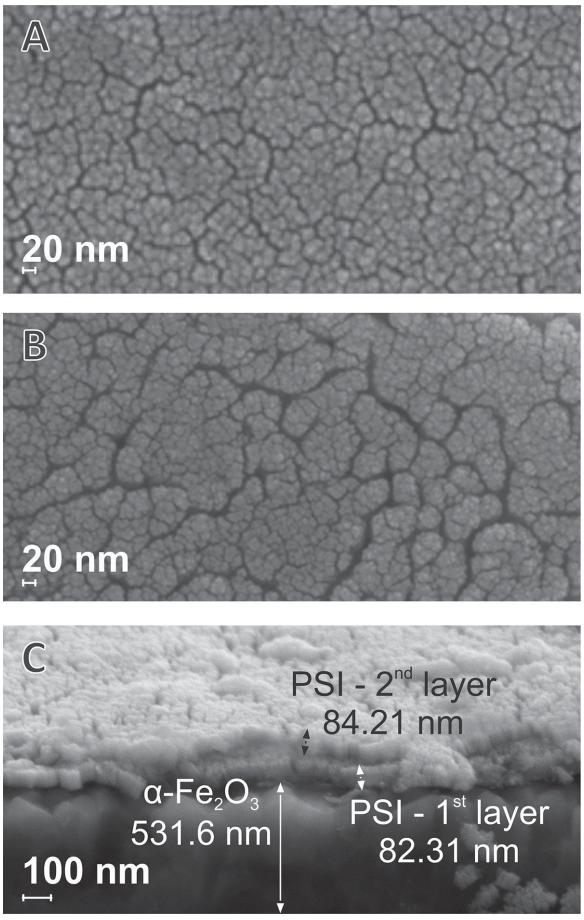

Figure 6. Electron microscopy imaging of biohybrid semiconductor photoanodes. Top view FE-SEM images of A) PSI/TiO_2/FTO electrodes, B) PSI/α-Fe_2O_3/FTO electrodes (PSI immobilization at pH 4). Cross-sectional FE-SEM image in C) corresponds to PSI/α-Fe_2O_3/FTO electrode; bottom-up: α-Fe_2O_3 and PSI-LHCI multilayer immobilised at pH 4 (physisorbed first layer and chemically cross-linked second layer are indicated).

cross-linking with hematite.[40] Time resolved fluorescence decay associated spectroscopy (FDAS) of the PSI-LHCI supercomplex in solution and upon its immobilization on the hematite/FTO photoanode additionally confirmed similar kinetics of energy transfer in both samples, albeit with the fastest ps decay component 2.5-fold slower for the immobilized PSI-LHCI supercomplex (see **Figure 8** and **Table 3**). This might be due to some distortion of the protein structure upon immobilization on the hematite surface, which could increase the distance between the pigments without affecting the overall functionality of PSI.

2.4. Sustained Photoelectrochemical H_2 Production Using PSI-LHCI-sensitised α-Fe_2O_3/FTO Photoanode within a Photoelectrochemical Cell

Next we examined the PSI-LHCI-functionalized hematite material as a photocatalyst for the photodriven reduction of protons to molecular hydrogen. Hematite is known to be a photocatalyst for water oxidation at wavelengths <600 nm,[26] whereas

© 2014 WILEY-VCH Verlag GmbH & Co. KGaA, Weinheim

ADVANCED FUNCTIONAL MATERIALS
www.afm-journal.de

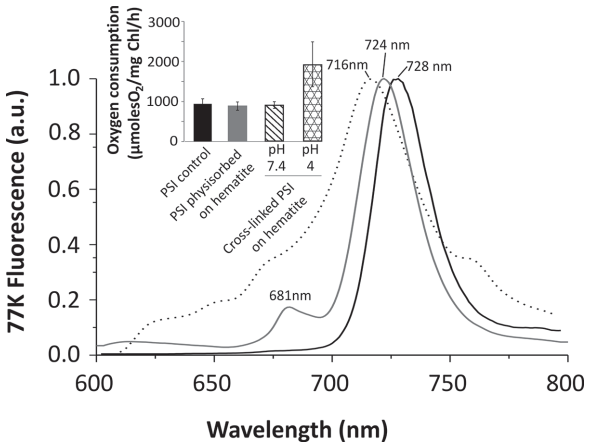

Figure 7. 77 K Fluorescence properties of the biohybrid PSI-hematite based photoanode. The maxima of fluorescence emission of PSI-LHCI chemically cross-linked and/or physisorbed onto hematite were at 724 nm (grey) and 716 nm (dotted black) respectively, whereas of PSI-LHCI in solution was at 728 nm (black). Observed shifts of immobilized PSI-LHCI are likely caused by the surface effect. Photocatalytic activity of immobilized PSI-LHCI (inset) was unaffected or enhanced upon immobilization.

PSI has a maximum absorption at 680 nm. As we were mainly interested in the contribution of PSI to light harvesting of the photoanode, photocatalysis was performed with light above 590 nm, minimizing the photocatalytic water splitting driven by hematite. The photocatalytic production of hydrogen from these experiments can therefore be attributed to the light harvesting capacities of the PSI-LHCI undergoing efficient electronic coupling with the semiconductor substrate. In an additional control experiment, we used α-Fe_2O_3/FTO slides without PSI-LHCI. We used electrodes composed of hematite that was functionalised with PSI-LHCI at pH 4, since we expected the most favorable orientation of this complex with respect to hematite, i.e., with the acceptor (reducing) side in close proximity of the semiconductor surface.

At a bias potential of 0.5 V only a small current and a negligible amount of hydrogen were observed when the sample was shielded from light (see **Figure 9**). Upon illumination with light above 590 nm, an anodic photocurrent of 4.2×10^{-6} A cm^{-2} was observed for the PSI-LHCI/α-Fe_2O_3/FTO electrode. The generation of this anodic photocurrent was accompanied by sustained photoelectrochemical H_2 production on the Pt counter electrode. The control photoanode that did not contain the PSI-LHCI complex produced a 2-fold reduced photocurrent of 2×10^{-6} A cm^{-2}. The low but measurable current is most likely due to the residual photocatalytic activity of hematite at 590–600 nm wavelengths. In this experiment only a trace amount of hydrogen was detected (see Figure 9) in contrast to the experiments that used light above 408 nm (data not shown), in line with the low photocatalytical activity of hematite at wavelengths above 590 nm. We estimated that at a bias potential of 0.5 V, the maximal rate of photodriven H_2 production on the Pt cathode using PSI-LHCI/hematite/FTO photoanode was 744 μmoles H_2 mg Chl^{-1} h^{-1}, representing one of the highest values obtained for PSI-based solar-to-fuel nanodevices.[4]

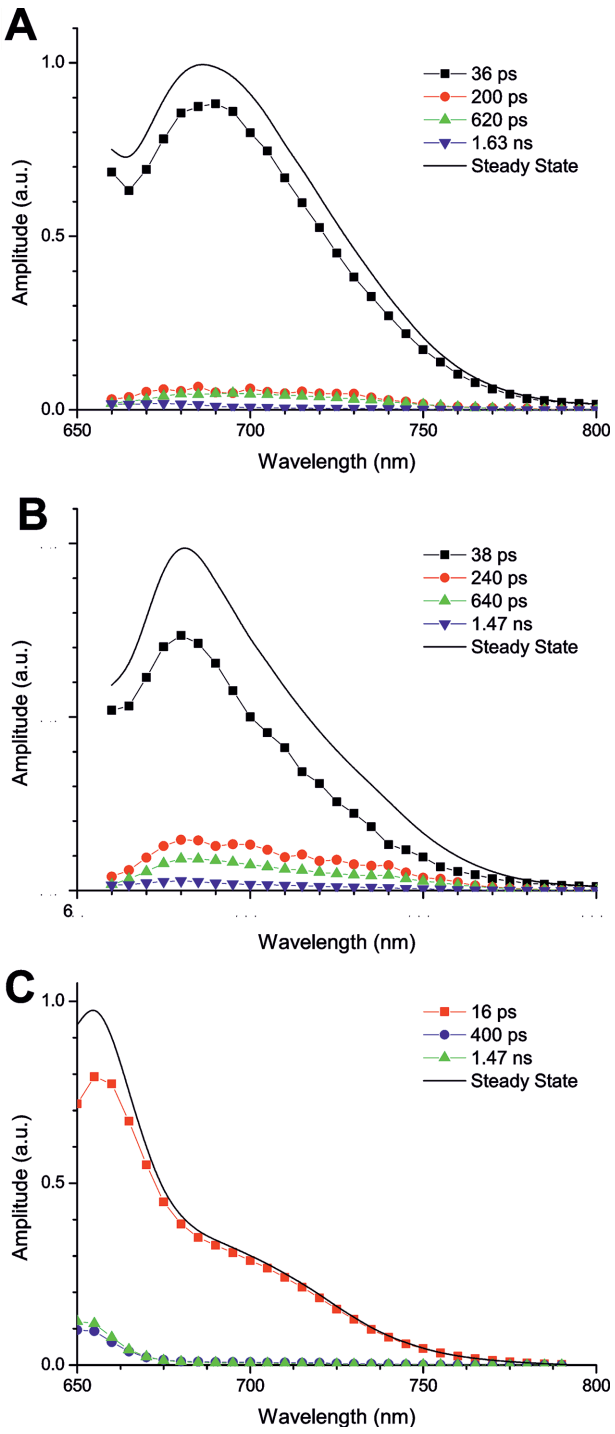

Figure 8. Fluorescence decay associated spectra (FDAS) of PSI-LHCI physisorbed on α-Fe_2O_3/FTO (A), cross-linked PSI-LHCI on α-Fe_2O_3/FTO (B), and PSI-LHCI in PBS, pH 7.4 (C). λex = 637 nm.

3. Conclusions

We constructed the nanostructured PSI-LHCI-functionalized hematite photoanode that exhibited an improved photoanodic current generation and was capable of photoelectrochemical

© 2014 WILEY-VCH Verlag GmbH & Co. KGaA, Weinheim

Table 3. Lifetime components obtained after global analysis of the *C. merolae* PSI-LHCI fluorescence decay upon immoblisation on hematite surface.

Sample	τ_1, ps	τ_2, ps	τ_3, ps	τ_4, ps	Global χ^2
1[a)]	36 ± 3	200 ± 90	620 ± 30	1630 ± 50	1.0064
2[b)]	38 ± 4	240 ± 20	640 ± 30	1470 ± 20	1.0206
3[c)]	16 ± 2	-	400 ± 30	1470 ± 10	0.9910

[a)]physisorbed PSI-LHCI/α-Fe_2O_3/FTO; [b)]cross-linked PSI-LHCI/α-Fe_2O_3/FTO; [c)]PSI-LHCI in phosphate buffer, pH 7.4. λ_{ex} = 637 nm.

hydrogen evolution compared to the pristine hematite due to its large nanostructured photoactive surface area, extended spectrum of light absorption into the red region and most likely, stabilized charge separation within the hematite layer. By manipulating surface charge distribution within PSI-LHCI at various pH we achieved oriented immobilization of this complex with its reducing side towards the hematite surface followed by nanostructuring of the PSI-LHCI multilayer in which the subsequent layers of this complex were organized in the head-to-tail orientation. The PSI-LHCI/hematite photoanode was successfully integrated into an operational open-circuit DSSC that was characterized by a 2-fold improved solar-to-electric quantum efficiency compared to the biohybrid PSI-based DSSC device reported previously by Mershin et al.[31] Moreover, this biohybrid PSI-based hematite photoanode was capable of sustained photodriven H_2 production upon illumination with visible light above 590 nm, indicating functional integration of the natural photosensitizer with the hematite water-splitting catalyst.

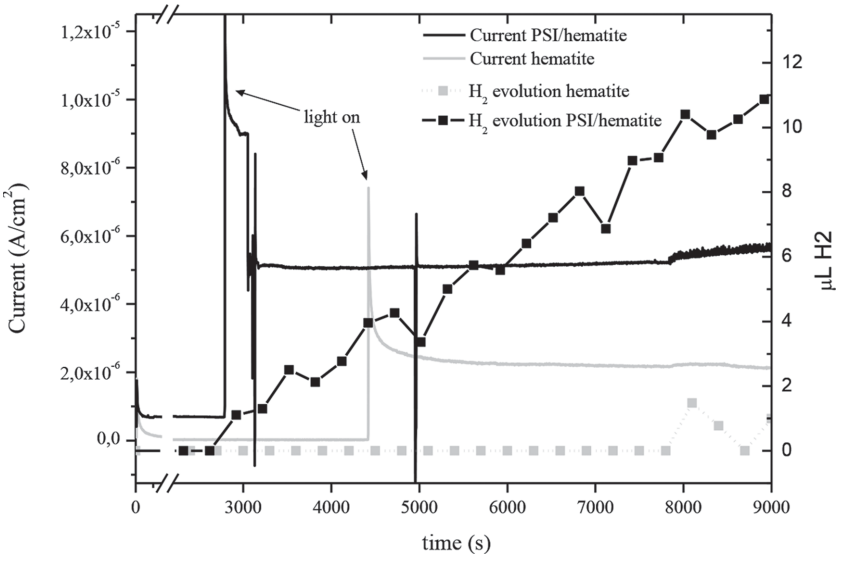

Figure 9. Generation of photocurrent and hydrogen evolution using PSI-LHCI-functionalised hematite photoanode and Pt cathode. Both electrodes were immersed in the phosphate buffer, pH 7.4. A bias potential of 0.5 V vs random Ag electrode was applied. A cut-off filter of >590 nm was used. The photoanode was irradiated from ~2800 seconds onwards. Current and hydrogen evolution curves from the control (α-Fe_2O_3/FTO) and PSI-LHCI/α-Fe_2O_3/FTO photoanodes are shown in grey and black, respectively.

4. Experimental Section

Materials: FTO glasses were purchased from Hartford Glass Company. TiO_2 coated FTO electrodes were purchased from Solaronix, and used after annealing at 450 °C for 30 min. Anhydrous solvents were either distilled from appropriate drying agents or purchased from Merck and degassed prior to use by purging with dry argon and kept over molecular sieves. All chemicals were purchased from commercial sources, and used as received. Iron (III) nitrate nonahydrate, oleic acid, agarose, 1,1′-carbonyldiimidazole (CDI), and 1 M phosphate buffer, pH 7.4 were purchased from Sigma-Aldrich. 1 M acetate buffer, pH 4 was purchased from Alfa Aesar.

Purification of C. merolae PSI-LHCI: Culturing of *C. merolae*, isolation of thylakoids and purification of crude PSI-LHCI was performed according to Krupnik et al.[42] Crude PSI (eluted from column DEAE TOYOPEARL 650M with 0.09 M NaCl) was concentrated on VivaSpin-20 (100,000 MWCO) concentrators to a volume of 1 ml and subsequently diluted to 50 ml with the carrier buffer (40 mM HEPES-KOH (Roth, Germany), pH 8, 3 mM $CaCl_2$, 25% (w/v) glycerol and 0.03% (w/v) *n*-dodecyl-β-D-maltoside (DDM) (Affymetrix, USA). The sample was applied onto the DEAE TOYOPEARL 650S column that was previously equilibrated with the same buffer. After washing the column with 3 CVs of the carrier buffer, pure PSI was eluted with a continuous 0–0.2 M NaCl gradient in the carrier buffer. The crude PSI-containing fractions were buffer-exchanged to 50 mM K_2HPO_4-KH_2PO_4 (Chempur, Poland), pH 8; 0.05% DDM and concentrated to 1 mg ml Chl^{-1}. Samples containing 0.5–1 mg Chl were applied onto a discontinuous sucrose gradient (0.4 M sucrose (Chempur, Poland), 0.45 M betaine (Sigma, Germany), 5 mM Tris-HCl (Chempur, Poland), pH 8, 0.05% (w/v) DDM) prepared by a freeze-thaw method,[43] and centrifuged at 125 000 xg (SW Ti32 rotor, Beckman-Coulter, USA) for 20 hours at 4 °C. The densest band containing pure PSI-LHCI supercomplex was concentrated to ~5 mg ml Chl^{-1} followed by exchange to the carrier buffer. Chl concentration was measured spectroscopically according to R. J. Porra et al.[44] using extinction coefficient of Chl*a* of 86.3 µl μg^{-1} cm^{-1}. Precise Chl content was determined from the standard curve (R^2 = 0.9999).

77 K Fluorescence Measurement: Steady-state Chl*a* fluorescence spectra were collected using a modified Shimadzu RF-5301PC spectrofluorometer[45] at 77 K and excitation wavelength of 440 nm. The control sample of PSI-LHCI (10 µg ml^{-1} Chl) in a buffer composed of 40 mM HEPES, pH 8, 3 mM $CaCl_2$, 25% (w/v) glycerol and 0.03% (w/v) DDM was loaded into pre-chilled cuvette, then frozen in liquid nitrogen for 5 min. in the dark prior to collecting emission spectra. The PSI-LHCI/hematite coated FTO slides were rigidly mounted onto the crystal extension of the optic pathway and the emission spectra were collected as above.

Photophysics: Time resolved fluorescence spectra of the PSI-LHCI supercomplex in phosphate-buffered saline (PBS) 7.4 solution as model and of the PSI immobilized on the semiconductor surface were collected by using the time correlated single photon counting (TCSPC) apparatus IBH System 5000 equipped with the TBX-05C photocathode. The samples were excited at 637 nm with the picosecond laser diode Hamamatsu SLHD-063 (typical pulse width <80 ps, intensity ca. 4×10^7 photons/pulse) operated at a repetition rate of 1 MHz by the stabilized picosecond light pulser Hamamatsu PLP-02, the channel resolution of the time to amplitude converter (TAC) was 6.5 ps. The kinetic traces were measured every 5 nm in the spectral region 650–800 nm. The fluorescence decay were analyzed by the global fitting module of the decay absorption spectra (DAS) 6.5 software (HORIBA Jobin Yvon), the traces were convoluted

© 2014 WILEY-VCH Verlag GmbH & Co. KGaA, Weinheim

with the measured instrumental response (fwhm ≈ 230 ps) and fitted to a sum of exponentials, $\Sigma A_i \exp(-t/\tau_i)$, the goodness of the 3- or 4-component fitting was evaluated by the global χ^2 parameter and weighted residuals. The wavelength dependences of the amplitudes of the individual kinetic components were plotted as fluorescence decay associated spectra (FDAS).

PSI Activity Measurement: Photochemical activity of the purified PSI-LHCI (5 μg Chl) was measured by the O_2 consumption assay[46,47] using an oxygen Clark-type electrode (Hansatech). Measurements were performed at 30 °C in the reaction buffer (0.5 M betaine, 40 mM HEPES, pH 8; 3 mM $CaCl_2$, 0.05% DDM) in the presence of 0.1 mM methyl viologen (Sigma, Germany) and 0.1 mM 2,6-dichloroindophenol (Koch Light Research Laboratories, England) as the exogenous electron acceptor and mediator, respectively. Samples (1 μg ml Chl^{-1}) were incubated in the dark for two minutes followed by addition of 3 mM sodium ascorbate (Roth, Germany) as the sacrificial electron donor and illumination with a white light intensity of 5,000 μE m^{-2} s^{-1}, using a KL 2500 LCD white light source (Schott, Germany). PSI-LHCI/hematite-coated slides were placed in a home-made measuring chamber, in the direction perpendicular and facing towards the light beam. For the PSI activity measurements, slides were submerged in 3 ml of the reaction buffer and the PSI activity was measured as above. Oxygen consumption activity of PSI was calculated from the initial rates of oxygen evolution curves. Chl was extracted from the PSI-LHCI-hematite slides with 80% acetone (v/v), then concentrated in a SpeedVac system (Waters, USA) at 30 °C and quantified by HPLC according to the method described by Krupnik et al.[42]

Calculation of the Surface Charge Map: The surface charge map was calculated for pH 7 and 4. All calculations were performed by the Swiss protein data bank viewer (SPDBV) 4.04 software available from the ExPASy database. The structural coordinates were taken from *Synechococcus elongatus* PSI, resolved at 2.5 Å.[7] Initial conditions for calculation were as described by Miteva et al.[48] For pH 7, surface charge map was calculated using the default settings for amino acids charge distribution available in the software. For pH 4 the net charge of amino acids was modified according to tabularized pK_a and pI values. Positively and negatively charged residues were rendered in blue and red, respectively. To determine the relationship between the average surface potential and surface charge, an algorithm described by Abraham-Shrauner (1973) was used.[49]

Preparation of Fe_2O_3 Sol–Gel: Fe_2O_3 sol–gel was prepared according to a modified method of Bora et al.[50] Briefly, the mixture of $Fe(NO_3)_3 \times 9H_2O$ (28 g) and oleic acid (17 g) was heated to 70 °C to give a homogeneous liquid phase. The temperature was increased to 125 °C and maintained for 90 min. to give a red-brown viscous homogeneous mixture which was then cooled down to room temperature, left for 24 h, and subsequently treated with 100 ml of tetrahydrofuran. The resultant solution was stirred for 30 min. and the powdery precipitate separated from the solution by centrifugation. After centrifugation, the supernatant (precursor complex) was recovered for subsequent coating.

Fabrication of α-Fe_2O_3/FTO Thin Films and Immobilization of PSI on the Semiconductor Surface: α-Fe_2O_3 thin films were prepared by dip coating of a sol–gel solution on a FTO coated glass substrate, followed by annealing at 550 °C for 2 h in air.[50] This deposition process was repeated once more and annealed at 550 °C for 30 min. α-Fe_2O_3 film deposited FTO was first treated with 0.5 M phosphate buffer, pH 7.4 for 2 h to obtain a net positively charged surface. In order to obtain polarized PSI with a negatively charged acceptor side, 200 μl of PSI-LHCI (4.13 mg Chl ml^{-1}) was dissolved in 1 ml 0.5 M acetate buffer, pH 4 and were kept for 6 h in the light. Alternatively, the PSI-LHCI sample was incubated in 0.5 M phosphate buffer, pH 7.4 in the dark. Subsequently, a 200 μl volume of this solution was dispersed over the hematite surface and kept for 12 h overnight in the dark at ambient temperature. In the preparation of the hematite–PSI conjugates by covalent cross-coupling, the hematite film readily adsorbed with PSI-LHCI was spin coated by 0.001% (w/v) agarose solution in order to decorate the surface with free hydroxyl groups.[51] The film was allowed to dry at room temperature prior to CDI activation. For the CDI treatment of the agarose-treated protein-coated hematite film, the agarose-modified electrodes were immersed CDI solution prepared in dioxane (50 mg CDI in 5 ml of dioxane) for 2 h at room temperature. To test the effect of dioxane on the photochemical activity of PSI-LHCI, the sample was incubated for 2 h in the dark at RT, in the presence of 1–10% (v/v) dioxane, resulting in a decrease of activity of 85–60%, respectively compared to an untreated control. When the reaction was completed, the electrode was rinsed 3 times with anhydrous toluene to remove excess CDI and reaction by-products.[51] The activated electrode was treated with a 0.5 M acetate buffer, and then was reacted with PSI-LHCI for 3 h at 37 °C on a hot plate with magnetic stirrer. After the conjugation reaction, the electrodes were rinsed with a washing buffer to remove unbound protein.

Construction of DSSCs: Sealed solar cell devices were prepared by immobilization of PSI-LHCI on the semiconductor electrodes (fabricated as in Ocakoglu et al.[51] Platinum-coated transparent counter electrode was prepared by a drop-casting of 0.05 M H_2PtCl_6 solution in isopropanol onto the FTO glass following a heat treatment at 450 °C for 15 min. Corresponding PSI-LHCI immobilized electrode and counter electrode are assembled into a sandwich type cell using a Surlyn polymer (Solaronix). The electrolyte, composed of 0.5 M lithium iodide and 0.05 M iodine in acetonitrile, was then introduced through pre-drilled holes in the counter electrode, which were sealed immediately with microscope cover slides and additional strips of Surlyn to avoid leakage.

Microscopic, X-ray Diffraction and Electrical Analyses: FE-SEM images were acquired using a Zeiss/Supra 55 FE-SEM, and the samples were platinum coated prior to FE-SEM measurements. The phase purity and structure of the semiconductor films were determined XRD analysis using a Bruker D8 Advanced powder diffractometer with a CuKα (0.15406 nm) radiation source. Current–voltage (*J–V*) measurements of the solar cells were performed using a KEITHLEY4200 semiconductor characterization system with a solar simulator. A long-pass filter with a 590 nm cut-off wavelength was used for the hematite-based DSSCs in order to eliminate visible light absorption of hematite under the simulated light. The different solar cell characteristics such as fill factor (*FF*) and overall energy conversion efficiency (η) were calculated using the following equations:[52]

$$FF = \frac{(J_{max} \times V_{max})}{(J_{sc} \times V_{oc})} \quad (1)$$

$$\eta = \frac{(V_{oc} \times J_{sc} \times FF)}{P_{in}} \quad (2)$$

where, J_{max} and V_{max} are the photocurrent and photovoltage for maximum power output, and J_{sc} and V_{oc} are the short-circuit photocurrent and open-circuit photovoltage, respectively. P_{in} is the power of incident light.

Amperometry and Hydrogen Evolution Measurement: For the hydrogen evolution experiments, a standard three electrode set-up was used, with Ag wire as a reference electrode, platinum coil as a counter electrode and the PSI-LHCI/hematite-coated FTO slide as a working electrode. The amperometric measurements were conducted using a PGSTAT 10 potentiostat (Autolab). A 3.6 cm^2 area of each electrode analyzed was submerged in a deoxygenated phosphate buffer (pH 7.2) in an air-tight glass vessel. To measure H_2 production, the headspace of the vessel was continuously pumped through the gass chromatography (GC) column with 5 Å molecular sieves for gas separation (Compact GC, Interscience). The GC samples were probed every 5 min. A 500 W Hg-Xe lamp (Hamamatsu, L8288) was used for the photocatalysis, using a water filter (path length of 30 cm) to eliminate IR radiation.

Acknowledgements

JK, TK and JJO gratefully ackowledge financial support by the Polish Ministry of Science and Higher Education and the European Science

© 2014 WILEY-VCH Verlag GmbH & Co. KGaA, Weinheim

Foundation (grant nr 844/N-ESF EuroSolarFuels/10/2011/0 to JK) and all the collaborations within the EUROCORES/EuroSolarFuels Solarfueltandem consortium. KO, EH, SY and FY thank The Scientific and Technological Research Council of Turkey, TUBITAK for the financial support (grant nr 110M803). AB and MPG thank the ESF-EUROCORES project EuroSolarFuels, the CNR project PM.P04.010 (MACOL) and the Progetto Bandiera N-CHEM for funding. BvdB and JNHR kindly acknowledge ESF-EUROCORES, NWO and Biosolarcell for financial contributions.

Received: April 30, 2014
Revised: August 1, 2014
Published online: October 2, 2014

[1] R. E. Blankenship, D. M. Tiede, J. Barber, G. W. Brudviq, G. Fleming, M. Ghirardi, M. R. Gunner, W. Junge, D. M. Kramer, A. Melis, T. A. Moore, C. C. Moser, D. G. Nocera, A. J. Nozik, D. R. Ort, W. W. Parson, R. C. Prince, R. T. Sayre, *Science* **2011**, *332*, 805–809.
[2] P. Yang, J. P. Tarascon, *Nat. Mater.* **2012**, *11*, 560–563.
[3] J. Kargul, J. Barber, *Molecular Solar Fuels*, 1st edition; RSC Publishing: Cambridge, **2012**; ch. 5, pp. 107–136.
[4] J. Kargul, J. D. Janna Olmos, T. Krupnik, *J. Plant Physiol.* **2012**, *169*, 1639–1653.
[5] A. Badura, T. Kothe, W. Schuhmann, M. Rögner, *Energy Environ. Sci.* **2011**, *4*, 3263–3274.
[6] K. Brettel, W. Leibl, *Biochim. Biophys. Acta (BBA) – Bioenergetics* **2001**, *1507*, 100–114.
[7] P. Jordan, P. Fromme, H. T. Witt, O. Klukas, W. Saenger, N. Krauss, *Nature* **2001**, *411*, 909–917.
[8] A. Ben-Shem, F. Frolow, N. Nelson, *Nature* **2003**, *426*, 630–635.
[9] A. Amunts, O. Drory, N. Nelson, *Nature* **2007**, *447*, 58–63.
[10] C. Slavov, M. Ballottari, T. Morosinotto, R. Bassi, A. R. Holzwarth, *Biophys. J.* **2008**, *94*, 3601–3612.
[11] S. Santabarbara, L. Galuppini, A. P. Casazza, *J. Integr. Plant Biol.* **2010**, *52*, 735–749.
[12] R. Das, P. Kiley, M. Segal, J. A. Norville, A. Yu, L. Wang, S. A. Trammell, L. E. Reddick, R. Kumar, F. Stellacc, N. Lebedev, J. Schnur, B. D. Bruce, S. Zhang, M. Baldo, *Nano Lett.* **2004**, *4*, 1079–1083.
[13] I. Carmeli, L. Frolov, C. Carmeli, S. Richter, *J. Am. Chem. Soc.* **2007**, *129*, 12352–12353.
[14] P. N. Ciesielski, C. J. Faulkner, M. T. Irwin, J. M. Gregory, N. H. Tolk, D. E. Cliffel, G. K. Jennings, *Adv. Funct. Mat.* **2010**, *20*, 4048–4054.
[15] P. N. Ciesielski, F. M. Hijazi, A. M. Scott, C. J. Faulkner, L. Beard, K. Emmett, S. J. Rosenthal, D. Cliffel, G. K. Jennings, *Bioresour. Technol.* **2010**, *101*, 3047–3053.
[16] P. N. Ciesielski, A. M. Scott, C. J. Faulkner, B. J. Berron, D. E. Cliffel, G. K. Jennings, *Nano Lett.* **2008**, *2*, 2465–2472.
[17] O. Yehezkeli, R. Tel-Vered, D. Michaeli, I. Willner, R. Nechushtai, *Photosynth Res.* **2014**, *120*, 71–85.
[18] A. Badura, D. Guschin, T. Kothe, M. J. Kopczak, W. Schuhmann, M. Rögner, *Energy Environ. Sci.* **2011**, *4*, 2435–2440.
[19] C. E. Lubner, R. Grimme, D. A. Bryant, J. H. Golbeck, *Biochemistry* **2010**, *49*, 404–414.
[20] C. J. Faulkner, S. Lees, P. N. Ciesielski, D. E. Cliffel, G. K. Jennings, *Langmuir* **2008**, *24*, 8409–8412.
[21] N. Terasaki, N. Yamamoto, T. Hiraga, Y. Yamanoi, T. Yonezawa, H. Nishihara, T. Ohmori, M. Sakai, M. Fujii, A. Tohri, M. Iwai, Y. Inoue, S. Yoneyama, M. Minakata, I. Enami, *Angew. Chem., Int. Ed.* **2009**, *48*, 1585–1587.
[22] N. Terasaki, N. Yamamoto, K. Tamada, M. Hattori, T. Hiraga, A. Tohri, I. Sato, M. Iwai, S. Taguchi, I. Enami, Y. Inoue, Y. Yamanoi, T. Yonezawa, K. Mizuno, M. Murata, H. Nishihara, S. Yoneyama, M. Minakata, T. Ohmori, M. Sakai, M. Fujii, *Biochim. Biophys. Acta, Bioenerg.* **2007**, *1767*, 653–659.
[23] O. Yehezkeli, O. I. Wilner, R. Tel-Vered, D. Roizman-Sade, R. Nechushtai, I. Willner, *J. Phys. Chem. B* **2010**, *114*, 14383–14388.
[24] K. Sivula, F. Le Formal, M. Graetzel, *Chem. Sus. Chem.* **2011**, *4*, 432–449.
[25] H. K. Mulmudi, S. K. Batabyal, M. Rao, R. R. Prabhakar, N. Matthews, Y. M. Lam, S. G. Mhasailkar, *Phys. Chem. Chem. Phys.* **2011**, *13*, 19307–19309.
[26] D. K. Bora, A. Braun, E. C. Constable, *Energy Environ. Sci.* **2013**, *6*, 407–425.
[27] M. Cavas, R. K. Gupta, A. A. Al-Ghamdi, Z. H. Gafer, F. El-Tantawy, F. Yakuphanoglu, *Mater. Lett.* **2013**, *105*, 106–109.
[28] M. J. Katz, S. C. Rihaa, N. C. Jeong, A. B. F. Martinson, O. K. Farha, J. T. Hupp, *Coord. Chem. Rev.* **2011**, *256*, 2521–2529.
[29] E. K. Park, M. Choi, J. H. Jeun, K. T. Lim, J. M. Kim, Y. S. Kim, *Microelectron. Eng.* **2013**, *111*, 166–169.
[30] F. Tam, G. P. Goodrich, B. R. Johnson, N. J. Halas, *Nano Lett.* **2007**, *7*, 496–501.
[31] A. Mershin, K. Matsumoto, L. Kaiser, D. Yu, M. Vaughn, Md. K. Nazeeruddin, B. D. Bruce, M. Graetzel, S. Zhang, *Sci. Rep.* **2012**, *2*, 1–7.
[32] M. Graetzel, R. A. J. Janssen, D. B. Mitzi, E. H. Sargent, *Nature* **2012**, *488*, 304–312.
[33] N. Tétreault, E. Horváth, T. Moehl, J. Brillet, R. Smajda, S. Bungener, N. Cai, P. Wang, S. M. Zakeeruddin, L. Forro, A. Magrez, M. Gratzel, *Nano Lett.* **2010**, *4*, 7644–7650.
[34] H. Han, P. Sudhagar, T. Song, Y. Jeon, I. Mora-Seró, F. Fabregat-Santiago, J. Bisquert, Y. Soo Kang, U. Paik, *Chem. Commun.* **2013**, *49*, 2810–2812.
[35] K. S. Joya, Y. F. Joya, K. Ocakoglu, R. van de Krol, *Angew. Chem., Int. Ed.* **2013**, *52*, 10426–10437.
[36] S. Rani, S. C. Roy, M. Paulose, O. K. Varghese, G. K. Mor, S. Kim, S. Yoriya, T. J. LaTempa, C. A. Grimes, *Phys. Chem. Chem. Phys.* **2010**, *12*, 2780–2800.
[37] K. Sivula, R. Zboril, F. Le Formal, R. Robert, A. Weidenkaff, J. Tucek, J. Frydrych, M. Grätzel, *J. Am. Chem. Soc.* **2010**, *132*, 7436–7444.
[38] I. V. Chernyshova, S. Ponnurangam, P. Somasundaran, *Phys. Chem. Chem. Phys.* **2010**, *12*, 14045–14056.
[39] A. Busch, J. Nield, M. Hippler, *Plant J.* **2010**, *62*, 886–897.
[40] D. K. Bora, E. A. Rozhkova, K. Schrantz, P. P. Wyss, A. Braun, T. Graule, E. C. Constable, *Adv. Funct. Mater.* **2012**, *22*, 490–502.
[41] K. Suttiponparnit, J. Jiang, M. Sahu, S. Suvachittanont, T. Charinpanitkul, P. Biswas, *Nanoscale Res. Lett.* **2011**, *6*, 1–8.
[42] T. Krupnik, E. Kotabová, L. S. Van Bezouwen, R. Mazur, M. Garstka, P. Nixon, J. Barber, R. Kan, E. J. Boekema, J. Kargul, *J. Biol. Chem.* **2013**, *288*, 23529–23542.
[43] J. Kargul, J. Nield, J. Barber, *J. Biol. Chem.* **2003**, *278*, 16135–16141.
[44] R. J. Porra, L. H. Grimme, *Anal. Biochem.* **1974**, *57*, 255–267.
[45] Ł. Rudowska, K. Gieczewska, R. Mazur, M. Garstka, A. Mostowska, *Biochim. Biophys. Acta* **2012**, *1817*, 1380–1387.
[46] S. I. Allakhverdiev, A. Sakamoto, Y. Nishiyama, M. Inaba, N. Murata, *Plant Physiol.* **2000**, *123*, 1047–1056.
[47] L. P. Vernon, S. Cardon, *Plant Physiol.* **1982**, *70*, 442–445.
[48] M. A. Miteva, P. Tufféry, B. O. Villoutreix, *Nucleic Acids Res.* **2005**, *33*, W372–W375.
[49] B. Abraham-Shrauner, *J. Colloid Interface Sci.* **1973**, *44*, 79–84.
[50] D. K. Bora, A. Braun, S. Erat, A. K. Ariffin, R. Löhnert, K. Sivula, J. R. Töpfer, M. Grätzel, R. Manzke, T. Graule, E. C. Constable, *J. Phys. Chem. C Nanomater. Interfaces* **2011**, *115*, 5619–5625.
[51] K. Ocakoglu, F. Yakuphanoglu, J. R. Durrant, S. Icli, *Sol. Energy Mater. Sol. Cells* **2008**, *92*, 1047–105.
[52] K. Wongcharee, V. Meeyoo, S. Chavadej, *Sol. Energy Mater. Sol. Cells* **2007**, *91*, 566–57.

© 2014 WILEY-VCH Verlag GmbH & Co. KGaA, Weinheim